Electronic Supplementary Information

A robust and active hybrid catalyst for facile oxygen reduction in solid oxide fuel cells

Yu Chen[a], Yan Chen[b,d], Dong Ding[a], Yong Ding[a], YongMan Choi[c], Lei Zhang[a], Seonyoung Yoo[a], Dongchang Chen[a], Ben deGlee[a], Han Xu[a], Qiyang Lu[b], Bote Zhao[a], Gulin Vardar[b], Jiayue Wang[b], Hendrik Bluhm[e], Ethan J. Crumlin[e], Chenghao Yang[d], Jiang Liu[d], Bilge Yildiz[b*], and Meilin Liu[a*]

[a]Materials Science and Engineering, Georgia Institute of Technology, Atlanta, GA 30332-0245, USA

[b]Laboratory for Electrochemical Interfaces, Department of Nuclear Science and Engineering and

Department of Materials Science and Engineering, Massachusetts Institute of Technology, 77

Massachusetts Avenue Cambridge, MA 02139, USA

[c]SABIC Technology Center, Riyadh 11551, Saudi Arabia

[d]New Energy Research Institute, School of Environment and Energy, South China University of

Technology, Guangzhou Higher Education Mega Center, Guangzhou, Guangdong, 510006, China

[e]Advanced Light Source, Lawrence Berkeley National Laboratory, Berkeley, California 94720,

United State

Experimental Section

Preparation of PNM, PrO_x and hybrid coating *solution for infiltration:*

Stoichiometric amounts of high-purity praseodymium nitrate hydrate, nickel nitrate hydrate, manganese nitrate hydrate (all from Alfa Aesar) were dissolved in DI water/ethanol mixture (volume ration is 1:1) to form 0.1M $Pr_2Ni_{0.5}Mn_{0.5}O_{4+\delta}$ (intened formula), $PrNi_{0.5}Mn_{0.5}MnO_3$(PNM) and $Pr(NO_3)_3$ solution. 5 wt.% polyvinyl pyrrolidone (PVP) were added to the solution as a surfactant and a stoichiometric amount of glycine was added as a complexing agent and the fuel for subsequent self-combustion. 5 μL of the stock solution was deposited on the porous LSCF cathode surface. The coatings were fired at 800 ^oC for 1 h during the cell start-up stage. The PNM powder was prepared by solution conbustion method. The ash was then fired at 800 ^oC for 5h. The phase compositions of PNM powders was determined by XRD (**Figure S1**).

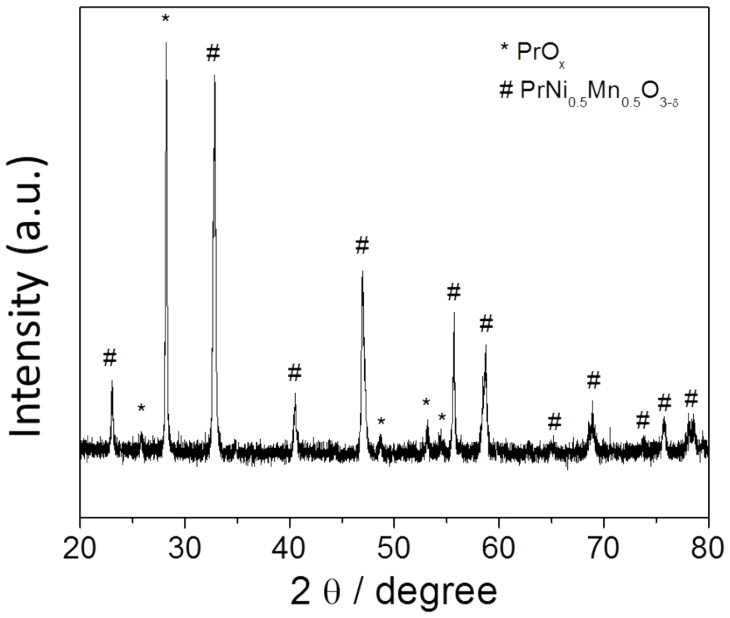

Figure S1. XRD pattern of a powder mixture derived from a glycine nitrate process, followed by firing at 800 ^oC in air for 5 h. The mixture was composed of PrO_x (Pr_7O_{12}, PDF# 01-071-0341) and PNM (a derivate from $PrMnO_3$, PDF# 01-085-2202)

Fabrication and characterization of pulsed laser deposition (PLD) model thin films:

To avoid the complication introduced by the surface microstruture, thin films prepared by PLD were used as a model system instead of porous electrode. LSCF thin film covered by a PrO_x, PNM and hybrid catalyst thin layer,with a thickness of around 10nm were grown on 8 mol% Y_2O_3-doped ZrO_2 (YSZ) (001) single crystal substrate. The PLD growth were carried out at 700 °C under oxygen pressure of 10 mTorr. A KrF excimer laser with a wavelength of 248 nm, energy of 400 mJ per pulse and a pulse frequency of 10 Hz was used for the deposition. The target substrate distance was set to be 7 cm. The films were cooled down to room temperature in 2 torr oxygen pressure with a cooling rate of 5 $^oC\ min^{-1}$. A GDC buffer layer was deposited between YSZ and LSCF to avoid the undesired chemical reactions. PrO_x, PNM and LSCF and hybrid sinlge layers were also grown under the same condition for comparision. As shown in Supplemeatary **Figure S2** and **Figure S3**, the PLD thin films was representative to the hybrid catalyst coated LSCF porous cathodes.

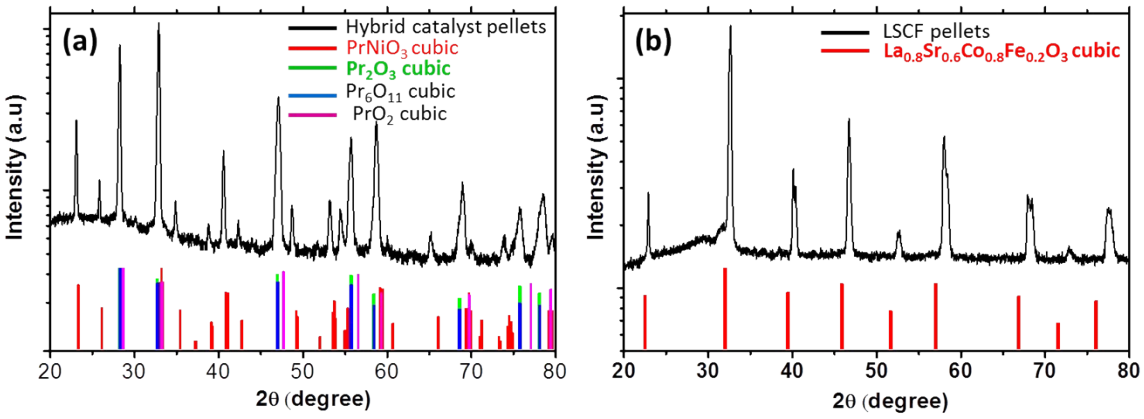

Figure S2. XRD patterns (2Θ - ω scan) of the PLD target for (a) hybrid catalyst and (b) bare LSCF. The hybrid catalyst and the LSCF target have the same phase composition as that of the porous hybrid catalyst coated-LSCF cathodes.

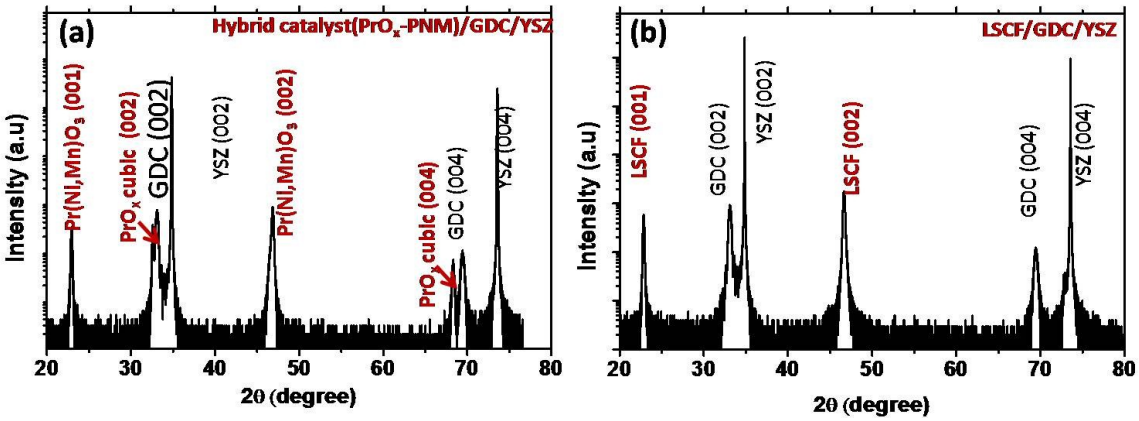

Figure S3. XRD patterns (2Θ - ω scan) of (a) hybrid catalyst film on YSZ with GDC as buffer layer, (b) LSCF on YSZ with GDC as buffer layer grown by PLD. The hybrid catalyst thin films are the mixture of fluorite PrO_x and perovskite PNM phase, which are the same as the porous cathodes. The targets were characterized using Panalytical Multipurpose Diffractometer. The PLD thin films were measured by HR-XRD using a Rigaku Smartlab diffractometer equipped with 2-bounce Ge (220) channel-cut monochromator and Cu Kα1 radiation. The surface morphology was characterized by atomic force microscopy (AFM) using Veeco/Digital Instrument Nanoscope IV. The AFM images were processed using the Nanoscope software version 5.31R1 (Digital Instruments).

The Near Ambient X-ray Photoelectron Spectroscopy (XPS) and Near Edge X-ray Absorption Fine Structure (NEXAFS) were carried out at Beamline 11.0.2 and Beamline 9.0.3 in partial electron yield detection mode at the Advanced Light Source, Berkeley.[1] Before all the characterization, the samples were heated at 300 ^{o}C in 200 mtorr oxygen for 1 hour to remove any carbon contamination.

Fabrication of symmetrical cells and single cells:

YSZ pellets were prepared by uniaxially pressing commercially available YSZ powders (Daiichi Kigenso, Japan) followed by sintering at 1450 ^{o}C for 5 h to achieve relative density of ~98%. LSCF (Fuelcell Materials, US) green tapes were prepared by tape-casting, which were then bound onto both sides of a YSZ electrolyte pellet using a slurry of SDC (function also as buffer layer). It is noted that GDC was used as buffer layer in our fabrication of thin film model cells. In both cases, a thin layer of ceria oxides (either GDC or SDC) were used as a buffer to prevent

chemical reactions between YSZ electrolyte and LSCF cathode at high temperatures. The cells were then co-fired at 1080 ^{o}C for 2 h to form porous LSCF electrodes (with an area of 0.316 cm^2) on YSZ. The SDC powder was synthesized using a chemical co-precipitation process. The SDC powder was then dispersed in acetone with V-006A (Heraeus, US) as binder and ball-milled for 24 h to form a stable SDC slurry.

Fabrication of anode-supported full cells :

Tape-casted NiO/YSZ anode support was first fabricated and pre-fired at 850 ^{o}C for 2 h. Then, a NiO/YSZ functional layer (~15 μm) and a YSZ electrolyte (~15 μm) were sequentially deposited on the anode support by a particle suspension coating process followed by co-firing at 1400 ^{o}C for 5 h. The LSCF cathode was then applied to the YSZ electrolyte using the same procedures as described earlier for the fabrication of symmetrical cells.

Characterization of phase composition and microstructure of cathodes:

Raman spectroscopy (Renishaw RM1000) was performed using 514 nm laser excitation on mixed bare LSCF and PNM-LSCF electrode before and after testing at 750 ^{o}C for 550 h. The microstructure and morphology of the LSCF pellets with/without catalysts coatings were examined using a scanning electron microscope (SEM, LEO 1530). The electronic structures of surface elements were characterized using X-ray photoelectron spectroscopy (Thermo K-Alpha XPS, Thermo Fisher Scientific).

Electrochemical measurements:

The area specific resistances (ASR) of cathodes were measured in a two electrode symmetric cell configuration using two pieces of Ag mesh as current collector (without Pt paste to avoid its possible contribution to catalytic activity) at 500–800 ^{o}C. Impedance spectra were acquired using a Solartron 1255 HF frequency response analyzer interfaced with an EG&G PAR potentiostat model 273A with an AC amplitude of 10 mV in the frequency range from 100 kHz to 0.01 Hz. The button cells were mounted on an alumina supporting tube for fuel cell testing at 750 ° C with humidified hydrogen (3% H_2O) as the fuel and ambient air as the oxidant. The cell

performance was monitored with an Arbin multi-channel electrochemical testing system (MSTAT).

Computational method

Periodic density functional theory (DFT) calculations were carried out using the Vienna ab initio simulation package (VASP)[2, 3] with the projector-augmented-wave (PAW) method[4]. Because the concurrent optimization of two effective *U* parameters (U_{eff}) of two B-site cations such as LSCF and PNM could result in incorrect results[5], we performed the spin-polarization method with the generalized gradient approximation (GGA) with using the Perdew-Burke-Ernzerhof (PBE)[6] exchange-correlation functional for LSCF and PNM. However, the PBE + *U* approach was applied for the comparison of the bulk and surface properties of fluorite-structure CeO_2 and PrO_2 to accurately describe the strong on-site Coulomb repulsion of the Ce and Pr 4f electrons with U_{eff} = 5.0 eV and 6.0 eV[7-9]. We constructed an orthorhombic structure with a kinetic energy cutoff for a plane wave basis set of 415 eV to simulate the oxygen-deficient perovskite LSCF and PNM. Monkhorst-Pack meshes[10] with the (3 × 3 × 3) and (3 × 3 × 1) were used for bulk and surface calculations, respectively. **Supplementary Table S2** summarizes the optimized lattice constants of LSCF and PNM. In this study, LSCF was built to understand the full coating of PNM on the LSCF cathode. To obtain the most probable surface, the surface stability of PNM(110) was examined since it was reported that ionic diffusion may take place most likely in the (110) direction[11]. The slabs for the 2-D surface calculations were separated by a vacuum space of 15 Å. As summarized in **Supplementary Table S4**, four types of PNM (110) are available, including Mn-PrO-Ni-PrO, Ni-PrO-Mn-PrO, PrO-Mn-PrO-Ni, and PrO-Ni-PrO-Mn. For this qualitative examination, one monolayer of PrO_x was deposited on PrO-Ni-PrO-Mn-terminated PNM(110) (**Supplementary Figure S18, S19**). Highly CPU-demanding optimization followed by transition-search calculations estimated that dissociated oxygen is incorporated an oxygen vacancy on the surface, and then reaches an oxygen vacancy site in the bulk phase. In this study, the oxygen-vacancy formation energy (E_{OV})[5, 12] was calculated by E_{OV} = E[defective surface] + 1/2E[O_2] – E[perfect surface], where E[defective surface], E[perfect surface], and E[O_2] are the predicted electronic energies for defective and perfect bulk structures and a gas-phase triplet O_2, respectively. The adsorption energy (E_{ad}) of O_2 on a surface was calculated by E_{ad} = E[O_2-surface]

– E[surface] – E[O_2], where E[O_2-surface] and E[surface] are the predicted electronic energies for an adsorbed O_2 species on a surface and a bare surface, respectively. Bulk diffusion barriers of E_a were calculated by $E_a = E_m + E_{OV}$, where E_m is a migration barrier of an oxygen ion through bulk phases.[13] E_m was determined by the climbing image-nudged elastic band (CI-NEB)[14] method.

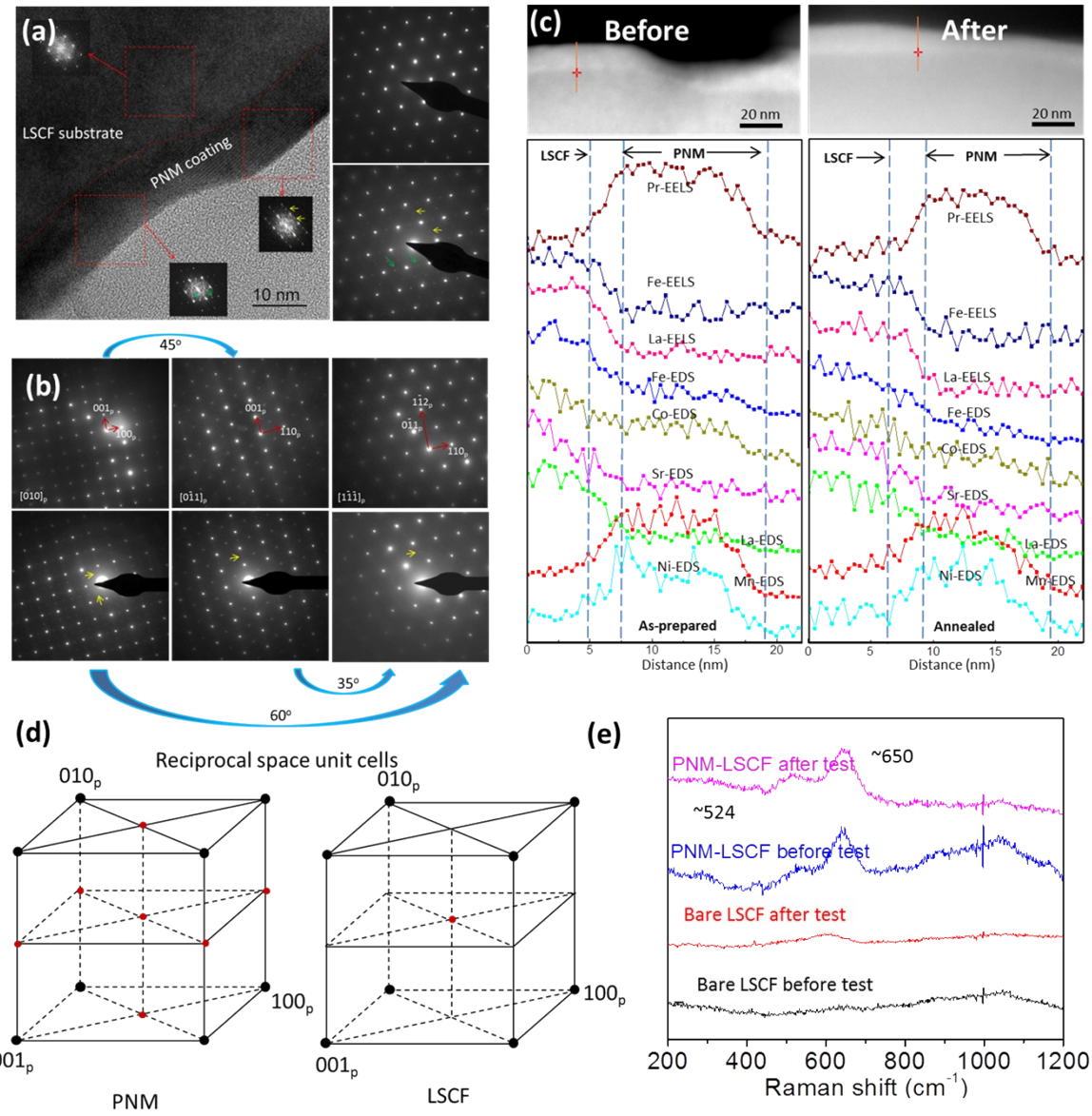

Figure S4. (a) a high-resolution TEM image of a PNM-coated LSCF pellet fired at 800°C for 2h; (b) selected-area electron diffraction (SAED) patterns from $[010]_p$, $[0\bar{1}1]_p$ and $1\bar{1}\bar{1}]_p$ electron-beam directions.Top three SAED patterns are solely from a LSCF grain, while the bottom three ones are from the epitaxial thin film area containing both LSCF and PNM grains. The subscript "p" means the primary perovskite unit cell; (c) HAADF-STEM images and elemental profiles along the lines for PNM-LSCF before and after annealling at 800°C for 2h; (d) the unit cells of PNM and LSCF in reciprocal space; (e) typical

Raman spectra of bare LSCF and PNM-coated LSCF cathodes (before and after test at 750^{o}C for 500h) collected in air at room temperature .

The red dotted line in **Figure S4a** highlights the interface between the LSCF and PNM. The coated PNM layer is around 10 nm thick. The epitaxial relationship between the PNM and LSCF can be clearly seen in the HRTEM image. The SAED patterns in the right-top and right-bottom come from the pure LSCF grain and the interface area, respectively. The arrowheads marked the superlattice diffraction spots come from the PNM phase. Although domains can be identified in the PNM film layer as revealed by the fast fourier transfer (FFT) from different thin film areas, both the LSCF and PNM share the same primary perovskite structure, which is corresponding to the strong diffraction spots in the SAED patterns. Figure S4**b shows the** selected-area electron diffraction (SAED) patterns from $[010]_p$, $[0\bar{1}1]_p$ and $[1\bar{1}\bar{1}]_p$ electron-beam directions. The top three SAED patterns are solely from a LSCF grain, while the bottom three ones are from the epitaxial thin film area containing both LSCF and PNM grains. The subscript "p" means the primary perovskite unit cell. Figure S4**c** shows the High Angle Annular Dark Field (HAADF) STEM image of LSCF with a PNM coating: before and after annealing at 800 ^{o}C for 500 h. The EELS and EDS ananlysis indicated that little diffusion was occured between the catalyst layer (10 nm thick) and the LSCF backbone; **Figure S4d shows** the unit cells of PNM and LSCF in reciprocal space. PNM is an orthorhombic structure (Space group: P n m a , Space group number: 62, with a= 5.3950Å, b= 7.6520Å, and c= 5.4460Å; Figure S4**e** shows the typical Raman spectra collected in air at room temperature for the cell (before and after test) with bare LSCF and PNM-coated LSCF. The bare LSCF electrode exhibits no obvious Raman bands since the vibration modes of pristine orthorhombic LSCF are not Raman active. The distortion could be preliminarily viewed as the unwanted structural change which may cause the gradual performance degradation. The pristine PNM-coated LSCF exhibited two obvious bands which contributed by active PNM surface coating. The band at ~650 cm^{-1} can be considered as the vibration of Mn-O bond in PNM lattice[15], whereras the band at ~524 cm^{-1} is result of Pr-O vibration in PNM lattice[16]. After the cell test, the Raman bands of PNM coating present no

observable changes. Also, no new bands corresponding to the LSCF substrate can be found, suggesting the structural stability and robustness of PNM-coated LSCF.

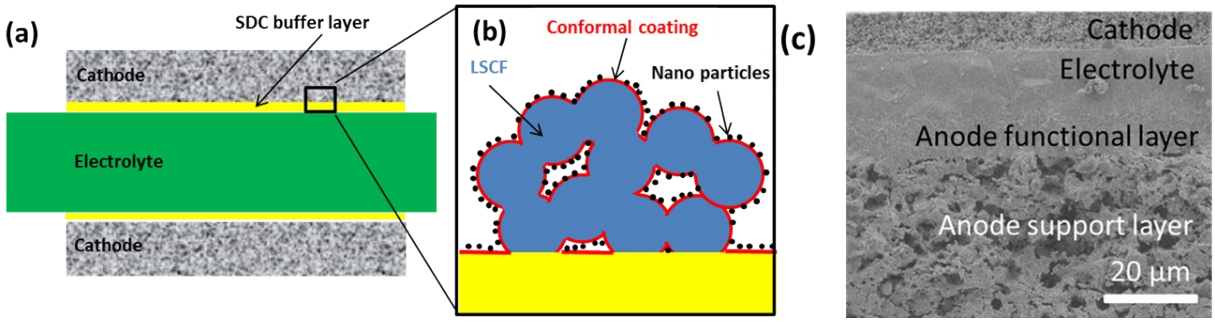

Figure S5. (a) Schematics of symmetrical cells with two indentical LSCF cathode backbones bonding to both sides of electrolyte with help of a SDC buffer layer; (b) Schematics of detailed LSCF coated with conformal catalyst coatings and nano particles; and (c) SEM image of as-prepared single cell, with configuration of NiO-YSZ anode support, NiO-YSZ functional layer (~15 µm), YSZ electrolyte (~15µm), SDC buffer layer (2-4µm) and hybrid catalyst coated LSCF cathode (50 µm).

It should be mentioned that the thinkness of our catalyst coating is very thin (from a few nm to about 20 nm), far thinner than other cell components such as cathode (~50 µm), electrolyte (~15 µm), and anode support (~800 µm). Accordingly, the amount of catalyst required is very small, implying that the Pr-based catalyst could be economically competitive for commercial applications.

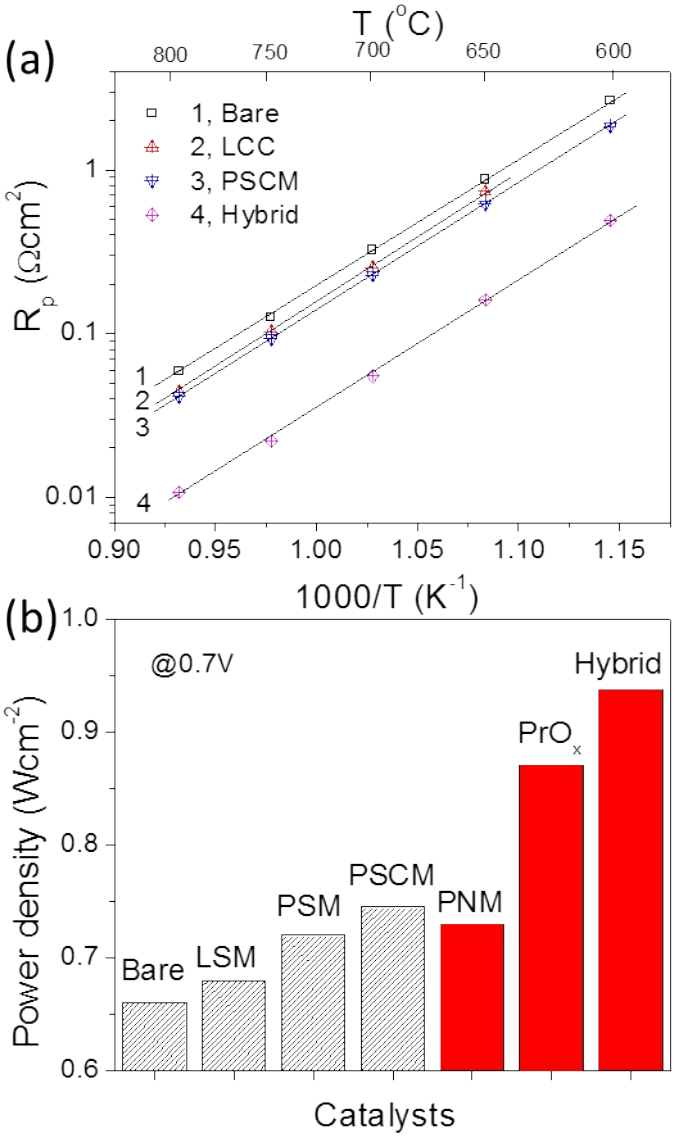

Figure S6. (a) Temperature dependence of interfacial polarization resistance (R_p) of different catalyst-coated LSCF cathodes under OCV conditions in ambient air: 1 Bare, 2 LCC[17], 3 PSCM[18] and 4 Hybrid; **(b)** Initial power density of cells with different catalysts coated LSCF cathode at 0.7V, using 3% water humidified H_2 as fuel and ambient air as oxidant: Bare, LSM[19], PSM[18], PSCM[18], and PNM, PrO_x-LSCF and Hybrid (this study).

Electrical Conductivity Relaxation (ECR) measurement

The surface exchange kinetics of catalyst coated LSCF were evaluated through electrical conductivity (ECR) relaxation measurement. Dense LSCF bar pellets were achieved by dry-

pressing the commercial LSCF powders at 300 MPa and sintering at 1250 °C for 5 h (the relative density > 95%). The sintered bars were polished by 1200 mesh SiC attrition paper to the dimension of approximately 2 x 2 x 13 mm and ultrasonically cleaned in ethanol. The catalyst solutions (0.01 M, nitrate precursor and glycine dissolved in 50 vol% ethanol-50vol% water solution) were coated on the entire polished surface with a firing process of 800 °C for 2 h with a projected coating thickness of 10 nm, estimated from the following equation[18]:

$$L = \frac{VCM}{\rho S}$$

where V is the volume of the solution, C is the solution concentration, M is the molar weight of the catalyst used for coating, ρ is the theoretical density of the infiltration material, and S is the surface area of LSCF bar that was coated with the solution.

The electrical conductivity was measured by the four probe DC method. A constant current (10 mA) was delivered to the two current wires, and the voltage response was recorded by a potentiostat instrument (MSTAT). Measurements were performed over the temperature range of 600 ~ 700°C. The sample was then heated to 750°C and hold for 1 h for equilibrium. The gas p_{O2} was varied by diluting the oxygen stream with argon [Ultra-pure grade, 99.999%, Airgas, GA, USA] Gas switching between two streams at the same measured flow rate was performed using a 4-way valve connected to the inlet line. The flow rate was maintained at 290 mL min^{-1}. In the ECR technique, the total conductivity of the sample is measured during an instantaneous step change in oxygen partial pressure (p_{O2}) at constant temperature. The gas p_{O2} was varied by diluting the oxygen stream with nitrogen. The gas pathways were included in the system, each with oxygen stream based argon stream, such that two different p_{O2} values could be simultaneously achieved. The gas flow rates for each p_{O2} stream were set with mass flow controllers. The change in electronic conductivity is directly related to p_{O2} through a proportional change in the concentration of charge carriers. For *p*-type conductors, the concentration of electron holes decreases directly with p_{O2}, resulting in decreased electronic conductivity as the bulk oxygen non-stoichiometry increases. The conductivity was normalized for each p_{O2} switch according to Eq. (1) and was fit to a solution of Fick's second law (Eqs. 2-4).

The variable parameters in the fit are the surface exchange coefficient, k_{chem}, measured in cm/s, and the bulk diffusion coefficient, D_{chem}, measured in cm^2/s.[20]

$$\sigma_n = \frac{\sigma_t - \sigma_0}{\sigma_\infty - \sigma_0} \tag{1}$$

$$\sigma_n = 1 - \sum_{m=1}^{\infty} \sum_{n=1}^{\infty} \sum_{p=1}^{\infty} \frac{2L_\beta^2 \exp\left(\frac{-\beta_m^2 D_{chem} t}{x^2}\right)}{\beta_m^2\left(\beta_m^2 + L_\beta^2 + L_\beta\right)} \times \frac{2L_\gamma^2 \exp\left(\frac{-\gamma_n^2 D_{chem} t}{y^2}\right)}{\gamma_n^2\left(\gamma_n^2 + L_\gamma^2 + L_\gamma\right)} \times \frac{2L_\phi^2 \exp\left(\frac{-\phi_p^2 D_{chem} t}{z^2}\right)}{\phi_p^2\left(\phi_p^2 + L_\phi^2 + L_\phi\right)} \tag{2}$$

$$L_\beta = x\frac{k_{chem}}{D_{chem}}; L_\gamma = y\frac{k_{chem}}{D_{chem}}; L_\phi = z\frac{k_{chem}}{D_{chem}} \tag{3}$$

$$\beta_m \tan\beta_m = L_\beta; \gamma_n \tan\gamma_n = L_\gamma; \phi_p \tan\phi_p = L_\phi \tag{4}$$

where t is time in seconds; σ_n is normalized conductivity (relative conductivity, g(t)), σ_t is instantaneous conductivity at time t, so is initial conductivity and σ_∞ is conductivity at equilibrium for a given p_{O2}; x, y, z are dimensions of the sample in centimeters, and β_m, γ_n, Φ_p are the positive, non-zero roots of Eq.(4) All calculations are carried out with ECRTOOLS a freely available MATLAB toolbox which allows the estimation of k and D from ECR data, the evaluation of the quality of the estimated parameters[21, 22].

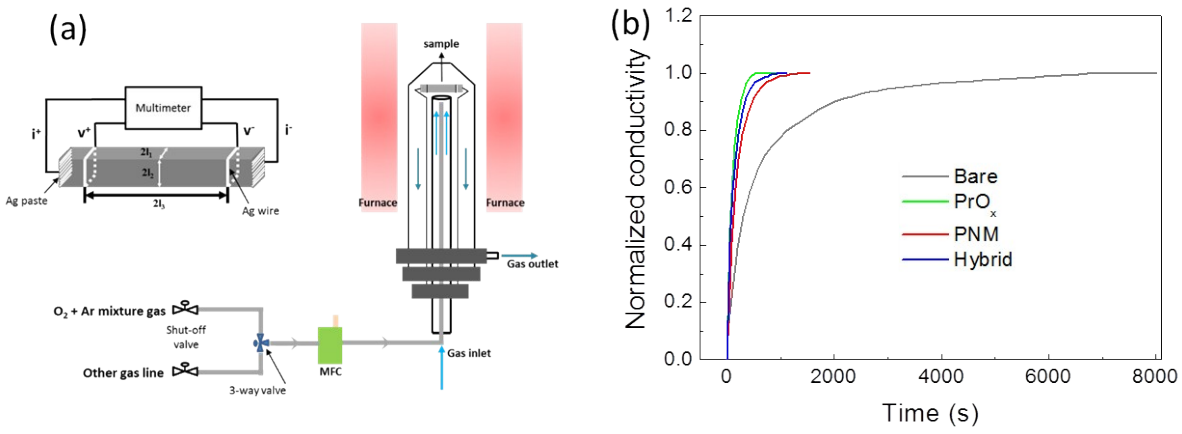

Figure S7. (a) Schematics of experimental arrangement for measuring ECR curves; (b) Normalized conductivity at 700 °C as a function of time for the bare LSCF and the catalysts coated on the LSCF (PrO_x, PNM and Hybrid), respectively. The relaxation time to reach equilibrium was about 7500 s for the bare LSCF bar pellet. Time was reduced to 1000-2000 s when the catalysts were coated on the LSCF bar pellet. The reduced relaxation time is attributed to enhance in the surface exchange properties.

For the electrical conductivity measurement, the experimental temperature was adjusted over the range from 300 to 900 °C. At each temperature point, a cumulative current load was applied to the two current wires, and the corresponding voltage response on the two voltage wires was recorded with a potentiostat instrument and EG&G 5210 amplifier. Electrical conductivity values were then calculated from the slope of the obtained straight line. As for the determination of *D* and *k*, electrical conductivity relaxation (ECR) was conducted between 550 and 750 °C at an interval of 50 °C. The bars were first stabilized at the given temperatures for approximately 1 h to ensure that they completely equilibrated with the surrounding atmosphere (p_{O2} = 0.21 atm), which was then abruptly switched to an alternative atmosphere (p_{O2} = 0.1 atm), thereby leading to a change in electrical conductivity. The change in conductivity with time was plotted as [σ(t) - σ(0)]/[σ(∞) - σ(0)]. Oxygen surface exchange coefficient (k) was calculated from the ECR curves by ECRTOOLS [23-25].

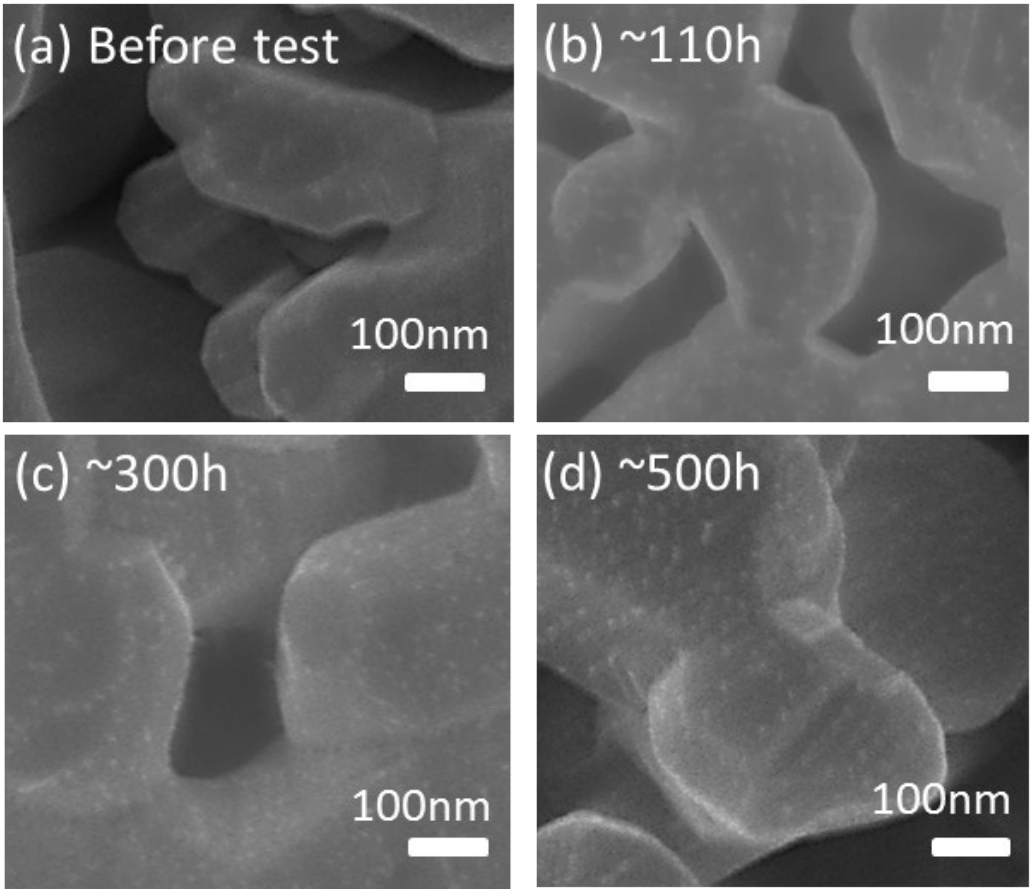

Figure S8. Morphological evolution of the hybrid catalyst coated LSCF cathode during the stability test at 750^{o}C at a cell voltage of 0.7 V as a function of operation time : (a) before test; (b) ~110h; (c) ~300h, and (d) ~500h. The essential morphological features remain unchanged, indicating reasonable stability of the electrodes.

In the first ~110 h of testing, it appears that more PrO_x particles were exsolved from the parental coating, which is beneficial to the performance enhancement since the oxygen-vacancy-rich surfaces of PrO_x nanoparticles may accelerate the rate of ORR. After 110h's testing, however, the morphology became reasonably stable, which is consistent with the observation that the power output became stable after ~110h operation (Figure 2d).

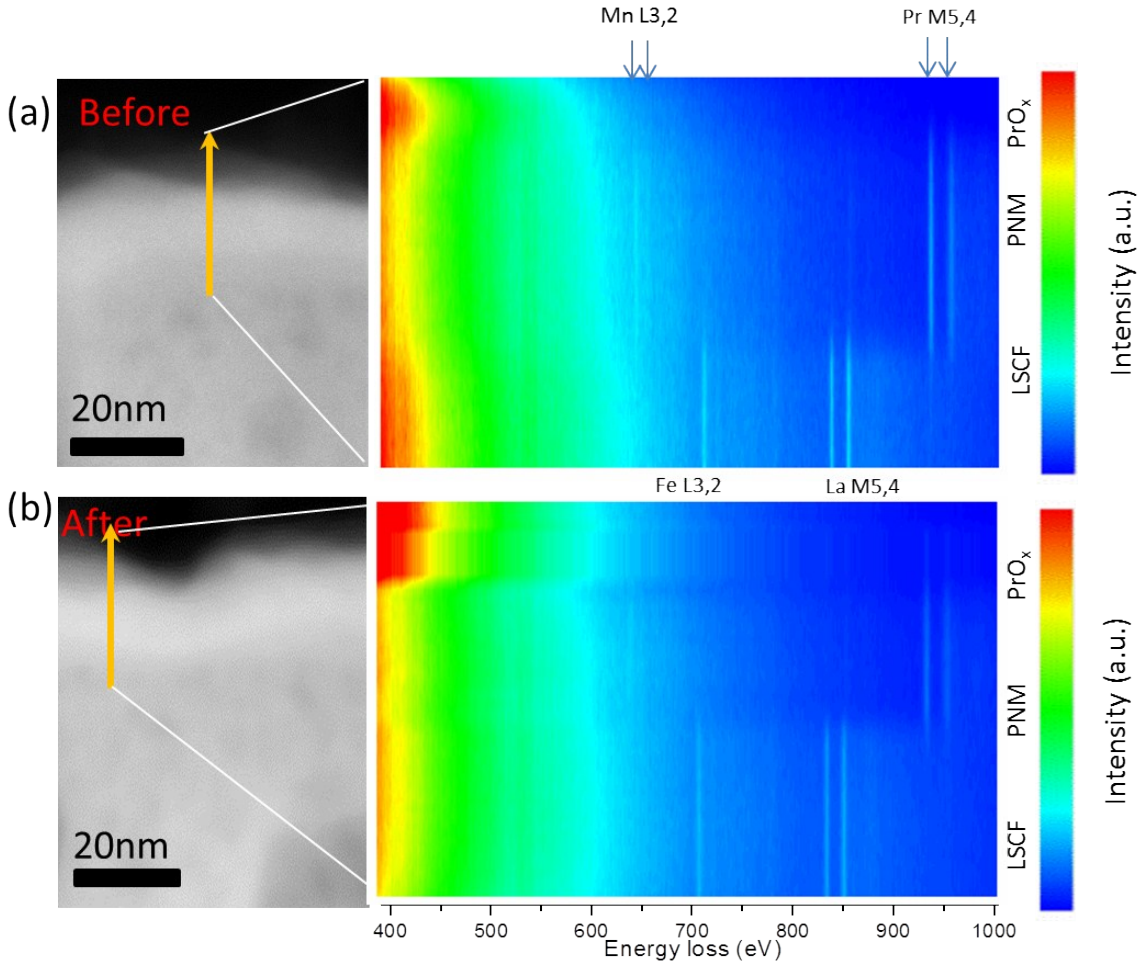

Figure S9. EELS spectra of hybrid catalyst coated LSCF along the orange line before (a) and after (b) stability test at 750 °C for ~500h.

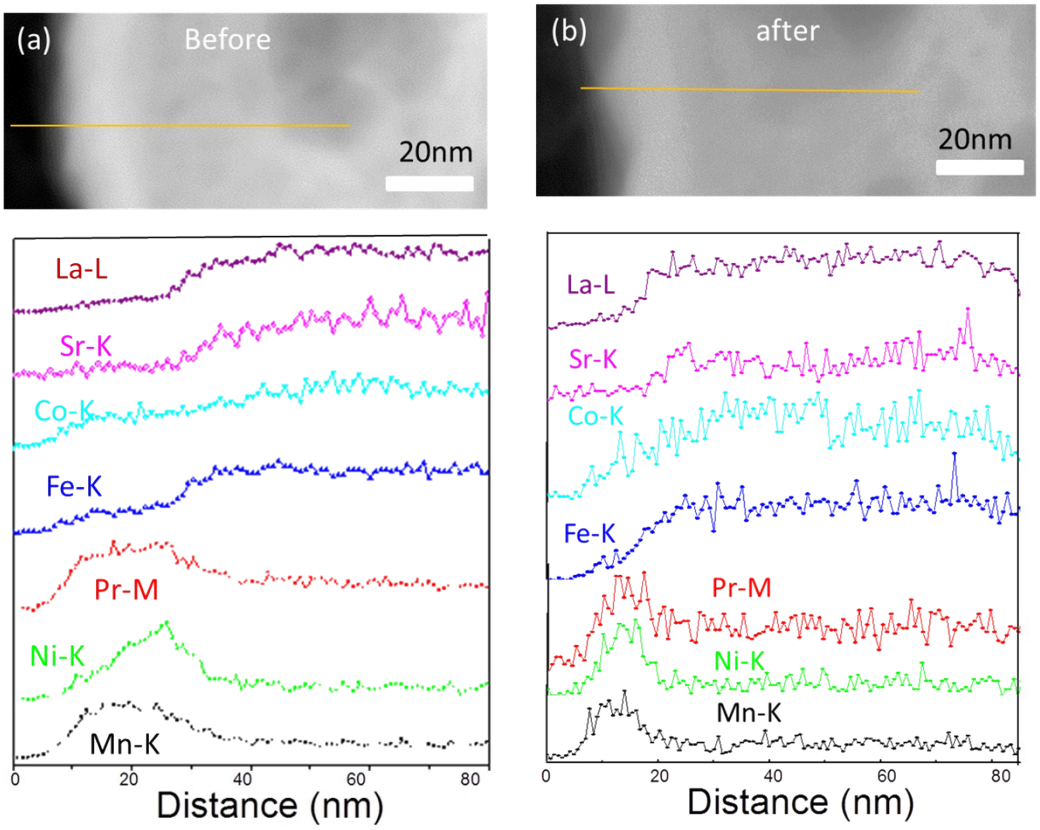

Figure S10. EDS profiles along the orange line of the cross-section of a hybrid catalyst coated-LSCF before (a) and after (b) the stability test at 750 °C for ~550 h. The signal became slightly noisier after the stability test, suggesting that there may be some inter-diffusion between the catalyst layer and the LSCF substrate. However, the essential composition of each layer still remained largely unchanged, implying reasonable stability during the test.

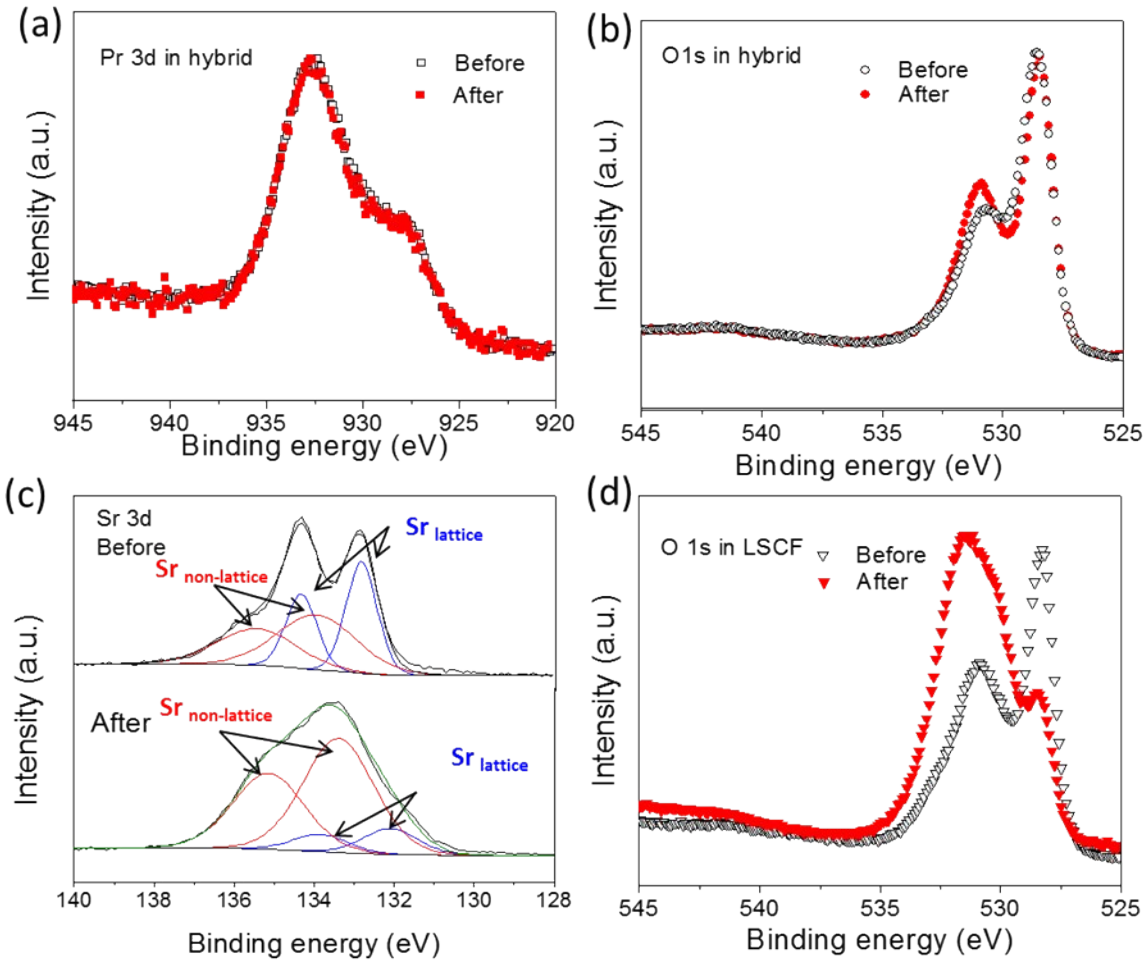

Figure S11. XPS spectra of (a) Pr 3d and (b) O 1s of the hybrid catalysts coated-LSCF; (c) Sr 3d and (d) O 1s of the bare LSCF before and after the stability test at 750°C for 500 h. It is shown that surface of the hybrid catalyst coated-LSCF has much better stability than that of the bare LSCF.

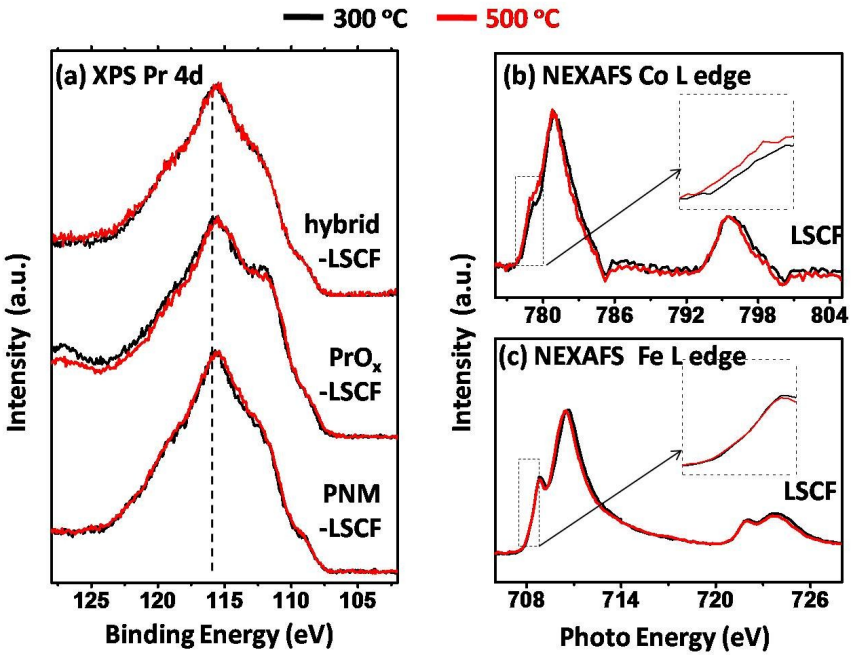

Figure S12. (a) XPS spectra of Pr 4d of PrO_x -, PNM- and hybrid catalyst coated LSCF; (b) Co L-edge (c) Fe L-edge absorption spectra of LSCF. The back and red curve are data collected at 300 °C and 500 °C, respectively, in 200 mtorr oxygen . The inset figure in (b) and (c) is the zoom in figure of the pre-edge region.

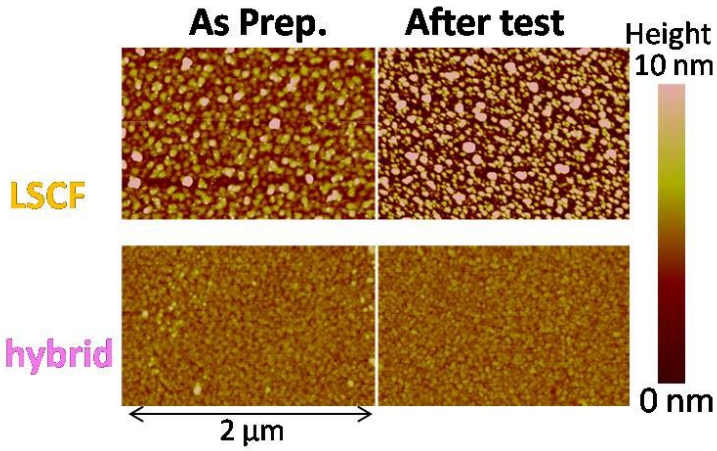

Figure S13. AFM image of LSCF and hybrid catalyst (PNM-PrO_x) thin films before and after test shown in Figure 4.

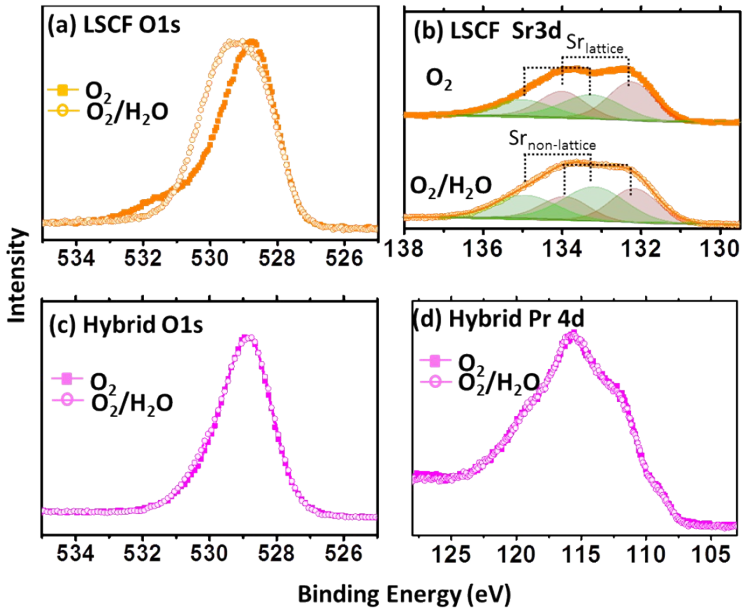

Figure S14. (a) O 1s and **(b)** Sr 3d spectra of the LSCF at 500 °C in 200 mtorr O_2 and with 10% H_2O. **(c)** O 1s and **(d)** Pr 4d spectra of the hybrid PNM-PrO_x catalyst at 500 °C in 200 mtorr O_2 and with 10% H_2O.

The main peak located near 528.8 eV is attributed to lattice O in LSCF[26, 27]. The small peak near 532 eV was due to the adsorbates at surface that have not been completely removed by heating at 300 °C. After exposing the sample to 10%H_2O+90%O_2, a clear increase in intensity was observed near 530 eV, which is attributed to -OH. Simultaneously, the component corresponding to Sr-OH ($Sr_{non\text{-}lattice}$) in Sr 3d spectra clearly increases after exposing the sample to 10%H_2O+90%O_2[26, 27] (**Figure S14b**), which is in accord with the change in the O 1s spectra (**Figure S 14a**). On the other hand, there appears little change in the O 1s and Pr 4d peak on the catalyst (pure) surface before and after exposure to 10% H_2O **(Figure S14c and d)**. As shown in **Supplementary Figure S15**, the O 1s and Pr 4d spectra for the hybrid catlalyst coated LSCF also do not change, indicating similarly stable surface for hybrid catlalyst coated LSCF samples.

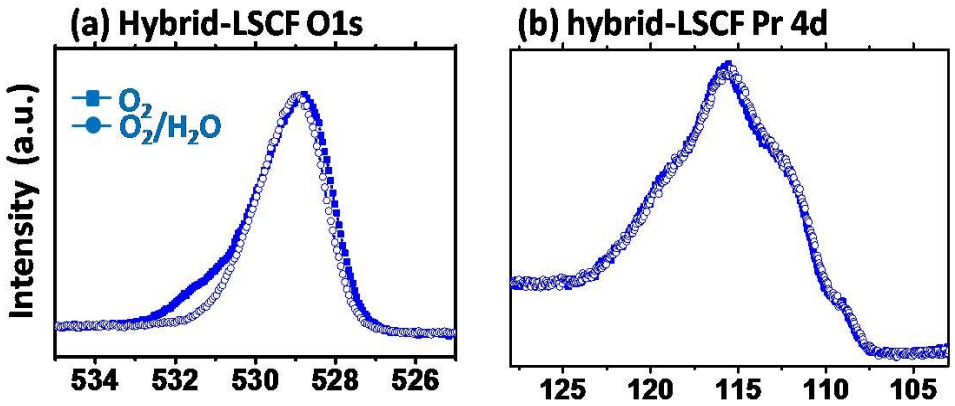

Figure S15. (e)O 1s and (f) Pr 4d spectra of hybrid catalyst coated LSCF at 500 °C in 200 mtorr O_2 and with 10% H_2O.

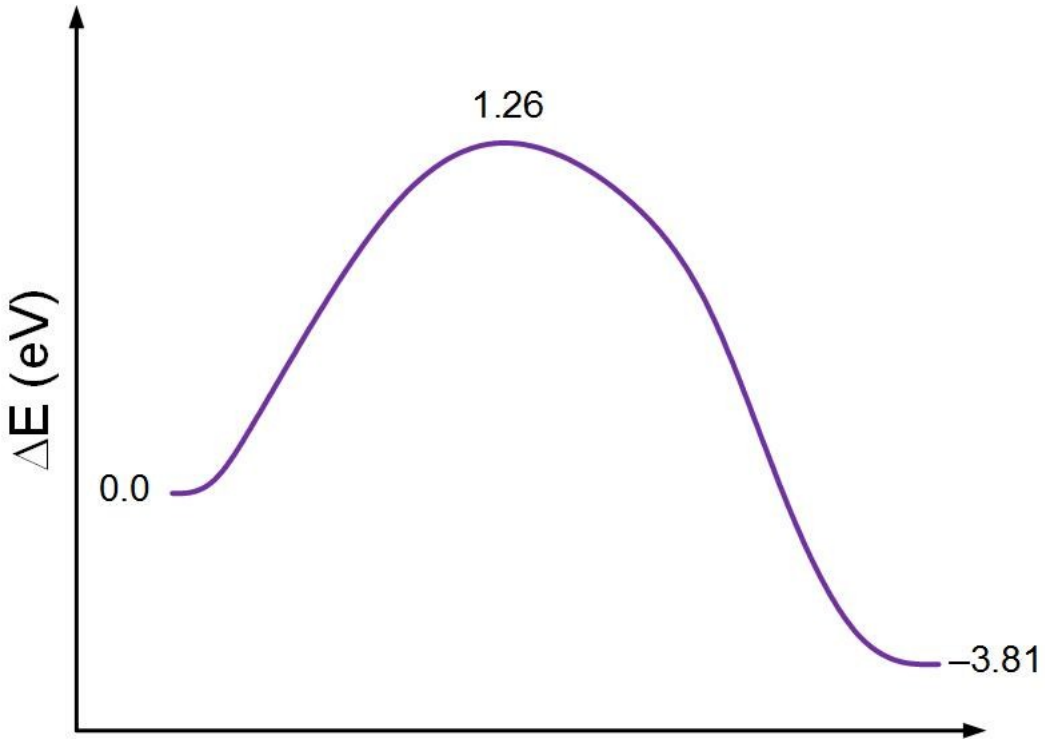

Figure S16. Trajectory of oxygen ion conduction through bulk PNM without Pr segregation. Note that the bulk diffusion with Pr segregation may take place without a well-defined migration barrier (0.45 eV).

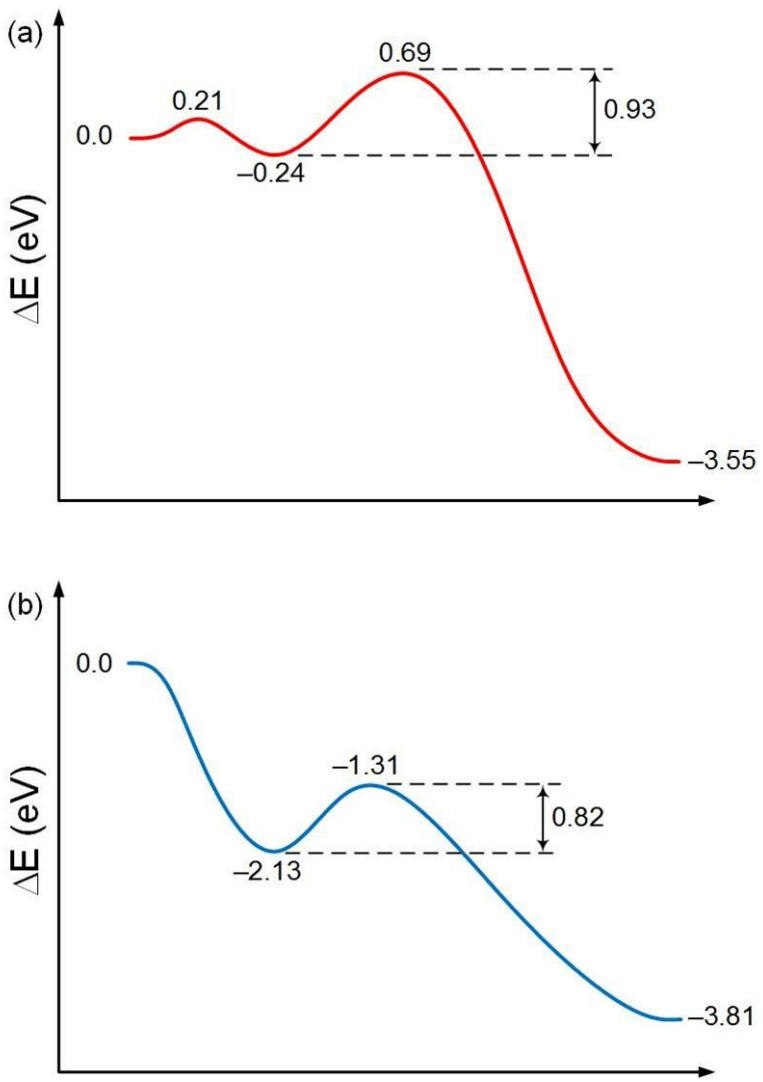

Figure S17. Trajectories of oxygen ion conduction through the PrO_x/PNM(001) surface (a) without and (b) with Pr segregation.

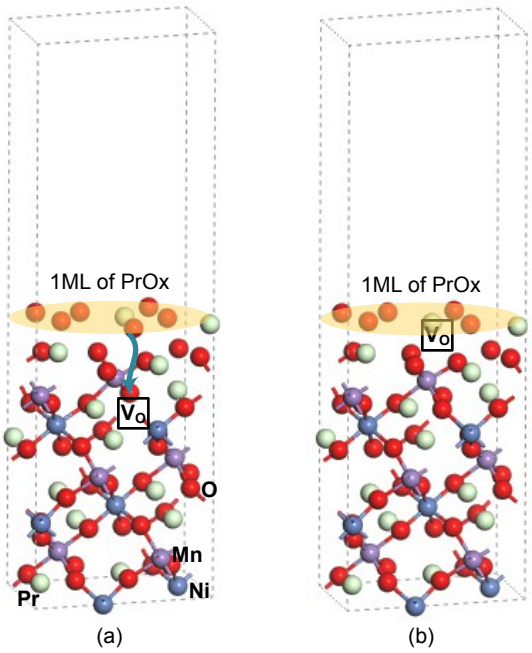

Figure S18. Schematic of oxygen ion diffusion from the surface of 1ML PrO_x into the PrO-Ni-PrO-Mn-terminated PNM(110) surface without Pr segregation. V_O represents an oxygen vacancy.

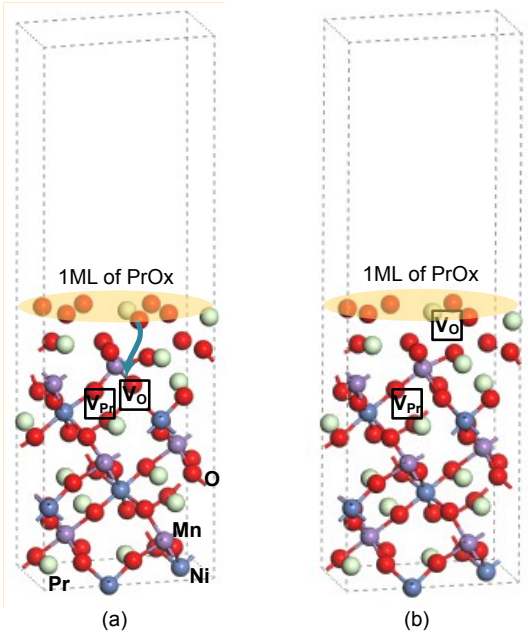

Figure S19. Schematic of oxygen ion diffusion from the surface of 1ML PrO_x into the PrO-Ni-PrO-Mn-terminated PNM(110) surface with Pr segregation. (a) Before and (b) after diffusion. V_O and V_{Pr} represent an oxygen vacancy and a Pr vacancy, respectively.

Table S1: Calculated lattice constants, averaged oxygen vacancy formation energies of bulk PrO_2 and CeO_2, and the adsorption energy of O_2 on PrO_2 and CeO_2 (111) surfaces.

	PrO_2	CeO_2	Remark
Lattice constants (Å)	a=b=c= 5.6716	a=b=c= 5.4680	Optimized GGA-PBE + *U*
Oxygen vacancy formation energy (E_{OV}) (eV)	1.04	4.69	U_{eff} = 6.0 eV and 5.0 eV for PrO_2 and CeO_2, respectively, using the bulk models of Pr_4O_8 and Ce_4O_8.
Adsorption energy (E_{ad}) on M (eV)	–1.19	~0.00	18-atomic layers of (111) are used by fixing the bottom 9 layers. The surfaces are oxygen-terminated (4 oxygen atoms on the surfaces).

Table S2: Calculated lattice constants and averaged oxygen vacancy formation energies of bulk PNM and LSCF.

	PNM	LSCF	Remark
Lattice constants (Å)	a = 5.5957 b = 7.5775 c = 5.4387	a = 5.5745 b = 7.5488 c = 5.4181	Orthorhombic type structures are used with $Pr_4Ni_2Mn_2O_{12}$ (PNM) and $La_2Sr_2Co_2Fe_2O_{12}$ (LSCF0.5) at GGA-PBE.
Oxygen vacancy formation energy (eV)	3.63	2.38	

Table S3: Calculated averaged oxygen vacancy formation energies (E_{OV}), migration energies (E_m), and bulk diffusion barriers (E_a) of bulk PNM*.

	Bulk structure without Pr segregation	Bulk structure with Pr segregation	Remark
Averaged oxygen vacancy formation energy (eV)	3.63	1.17	
Migration energy (eV)	1.26	0.45	
Bulk diffusion barrier (eV)	4.89	1.62	

*Orthorhombic type structures were used with $Pr_4Ni_2Mn_2O_{12}$ and $Pr_3Ni_2Mn_2O_{12}$ at GGA-PBE.

Table S4: Calculated surface energies of PNM(110)*.

	Surface energy (J/m^3)
Mn-PrO-Ni-PrO	–2.04
Ni-PrO-Mn-PrO	–3.02
PrO-Mn-PrO-Ni	–3.24
PrO-Ni-PrO-Mn	–3.38

*PNM(110) of $Pr_{12}Ni_6Mn_6O_{16}$ was applied with the vacuum space of 10 Å. The surface energies were calculated similar to the previous study[28].

References:

1. D. F. Ogletree, H. Bluhm, E. D. Hebenstreit and M. Salmeron, *Nucl Instrum Meth A*, 2009, **601**, 151-160.
2. G. Kresse and J. Hafner, *Phys. Rev. B*, 1993, **47**, 558-561.
3. G. Kresse and J. Furthmuller, *Phys. Rev. B*, 1996, **54**, 11169-11186.
4. P. E. Blöchl, *Phys. Rev. B*, 1994, **50**, 17953-17979.
5. Y. A. Mastrikov, M. M. Kuklja, E. A. Kotomin and J. Maier, *Energy & Environ. Sci.*, 2010, **3**, 1544-1550.
6. J. P. Perdew, K. Burke and M. Ernzerhof, *Phys. Rev. Lett.*, 1996, **77**, 3865-3868.
7. Z. Lu and Z. Yang, *J. Phys. Condens. Matter.*, 2010, **22**, 475003.
8. Y. Choi, M. Scott, T. Söhnel and H. Idriss, *Phys. Chem. Chem. Phys.*, 2014, **16**, 22588-22599.
9. F. Tran, J. Schweifer, P. Blaha, K. Schwarz and P. Novák, *Phys. Rev. B*, 2008, **77**, 085123.
10. H. J. Monkhorst and J. D. Pack, *Phys. Rev. B*, 1976, **13**, 5188-5192.
11. M. Saiful Islam, *J Mater Chem*, 2000, **10**, 1027-1038.
12. Y. Choi, M. C. Lin and M. Liu, *J. Power Sources*, 2010, **195**, 1441-1445.
13. D. A. Andersson, S. I. Simak, N. V. Skorodumova, I. A. Abrikosov and B. Johansson, *Proc. Natl. Acad. Sci. U.S.A.*, 2006, **103**, 3518–3521.
14. G. Henkelman, B. P. Uberuaga and H. Jónsson, *J. Chem. Phys.*, 2000, **113**, 9901-9904.
15. R. K. Gupta and C. M. Whang, *Journal of Physics: Condensed Matter*, 2007, **19**, 196209.
16. W. Y. Hernández, O. H. Laguna, M. A. Centeno and J. A. Odriozola, *Journal of Solid State Chemistry*, 2011, **184**, 3014-3020.
17. M. Liu, D. Ding, K. Blinn, X. Li, L. Nie and M. Liu, *International Journal of Hydrogen Energy*, 2012, **37**, 8613-8620.
18. D. Ding, M. Liu, Z. Liu, X. Li, K. Blinn, X. Zhu and M. Liu, *Advanced Energy Materials*, 2013, **3**, 1149-1154.
19. M. E. Lynch, L. Yang, W. Qin, J.-J. Choi, M. Liu, K. Blinn and M. Liu, *Energy & Environmental Science*, 2011, **4**, 2249-2258.
20. D. Chen and Z. Shao, *International Journal of Hydrogen Energy*, 2011, **36**, 6948-6956.
21. Z. Zhang, D. Chen, Y. Gao, G. Yang, F. Dong, C. Chen, F. Ciucci and Z. Shao, *RSC Advances*, 2014, **4**, 25924.
22. F. Ciucci, *Solid State Ionics*, 2013, **239**, 28-40.
23. L. Jiang, E. Morelius, J. W. Zhang, M. Wolcott and J. Holbery, *J Compos Mater*, 2008, **42**, 2629-2645.
24. F. Dong, M. Ni, Y. Chen, D. Chen, M. O. Tadé and Z. Shao, *J. Mater. Chem. A*, 2014, **2**, 20520-20529.
25. C. Xia, T. Hong and K. Brinkman, *ChemElectroChem*, 2016, DOI: 10.1002/celc.201500529, n/a-n/a.
26. E. J. Crumlin, E. Mutoro, Z. Liu, M. E. Grass, M. D. Biegalski, Y. L. Lee, D. Morgan, H. M. Christen, H. Bluhm and Y. Shao-Horn, *Energy Environ. Sci.*, 2012, **5**, 6081-6088.
27. Y. Chen, W. C. Jung, Z. Cai, J. J. Kim, H. Tuller and B. Yildiz, *Energy Environ. Sci.*, 2012, **5**, 7979-7988.
28. Z. Yang, T. K. Woo, M. Baudin and K. Hermansson, *The Journal of Chemical Physics*, 2004, **120**, 7741-7749.